

Unusual synchronization phenomena during electrodisolution of silicon: the role of nonlinear global coupling

Lennart Schmidt^{1,2}, Konrad Schönleber¹, Vladimir García-Morales¹,
and Katharina Krischer¹

¹Non-Equilibrium Chemical Physics - TU München ,
James-Franck-Str. 1, D-85748 Garching, Germany,
krischer@ph.tum.de ,

²Institute for Advanced Study - TU München, , Lichtenbergstr. 2a,
D-85748 Garching, Germany

1 Introduction

Complex spatiotemporal pattern formation is an intriguing phenomenon often observed in nature. An example in biological systems is the spontaneous emergence of plane and spiral calcium waves in stimulated *Xenopus* oocytes [1]. Even human-body related phenomena are known, such as electrical turbulence in the heart muscle [2, 3]. Spiral waves and their break-up could be observed in cardiac tissue and these phenomena could be explained from a solely dynamical point of view. Thus, for example, the spiral break-up is not triggered by inhomogeneities in the system, but rather arises via a dynamic instability. This immediately shows that there is a need for model systems to study the nonlinear dynamics in complex, pattern forming systems. Such a model system is the catalytic oxidation of carbon monoxide on a platinum surface in the UHV [4] exhibiting a variety of patterns, like spiral waves, pulses, solitons, target patterns and turbulence. Another model system is the Belousov-Zhabotinsky reaction, which became a prototypical system for the study of spiral dynamics, but gives also rise to standing, irregular and localized clusters under global feedback [5, 6].

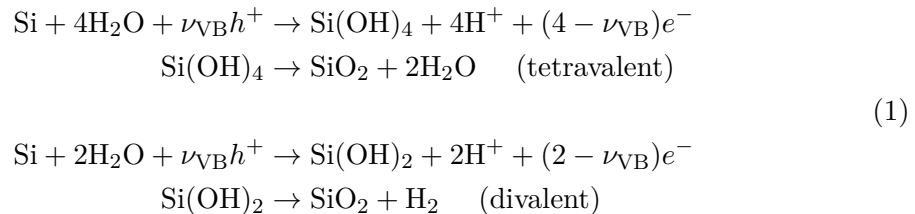
In this Chapter we present spatiotemporal dynamics found during the photoelectrodisolution of n-doped silicon and show that this experimental system is a convenient model system to study nonlinear dynamics with a conserved quantity: the mean-field of the two-dimensional oscillatory medium exhibits harmonic oscillations with constant amplitude and frequency. We model the experiments with an adapted version of the complex

Ginzburg-Landau equation [7, 8], which is the appropriate normal form close to a supercritical Hopf bifurcation. In order to capture the mean-field oscillations, one has to introduce a nonlinear global coupling into the equation. As we will show in what follows, this nonlinear global coupling and the resulting conservation law are the origin of a wide variety of spatiotemporal patterns. Even the coexistence of regions exhibiting distinct dynamical behaviors is observed for many parameter values.

2 Experimental system

The experimental system under consideration is the potentiostatic photoelectrodisolution of n-doped silicon under high anodic voltage in the presence of a fluoride containing electrolyte. In this process, the silicon is first electrochemically oxidized and the oxide layer is subsequently etched away purely chemically by the fluoride in the electrolyte. As a result of this interplay, depending on the external voltage, a stable oxide layer may form.

The anodic oxidation follows either a tetravalent or a divalent mechanism, where in both cases the first stage is an electrochemical and the second stage a chemical process [9, 10]:



Here ν_{VB} is the amount of charge carriers stemming from the valence band of the silicon. As the divalent oxidation mechanism is accompanied by H_2 evolution the relative prevalence of both oxidation valences can be well distinguished. A significant contribution of the divalent mechanism is only found for relatively low anodic voltages [11] and the reaction valency ν in the parameter regime considered in our work is close to $\nu = 4$ [12]. We will thus neglect the divalent oxidation pathway for the rest of this article.

The initial charge transfer step for the electrochemical oxidation is always the capture of a hole from the valence band of the silicon leading to $\nu_{\text{VB}} \geq 1$ in Eq.(1) [13]. In n-type silicon these holes have to be photo-generated. Electron injections into the conduction band can lead to an overall current higher than the one induced by the photon flux incident on the surface, i.e., to external quantum efficiencies larger than one [14]. This current multiplication effect increases with decreasing illumination intensity and the limiting value of $\nu_{\text{VB}} = 1$ has been experimentally realized in literature [14, 11]. While this trend is also present in our experiments, the values we typically find are in the range of $2 \leq \nu_{\text{VB}} \leq 4$.

The etching of the oxide is mainly due to the species HF and HF_2^- in dimolecular processes [15]. As the distribution of the fluorine to the species HF , HF_2^- and F^- is pH dependent and the rates for all dimolecular reaction pathways of the two etching species are different, the pH value as well as the total fluorine concentration c_{F} determine the

total etch rate. It is thus possible experimentally to vary the etch rate as well as the dominant etching pathway by the variation of the pH value of the solution and c_F . Especially the voltage dependence of the etch rate is expected to show some variation with the distribution of the fluorine to the respective solvated species as HF_2^- and F^- are charged but HF is not.

A typical cyclic voltammogram of a silicon electrodisolution process together with a measure of the total mass of the corresponding oxide layer ξ is shown in Fig. 1a. Below

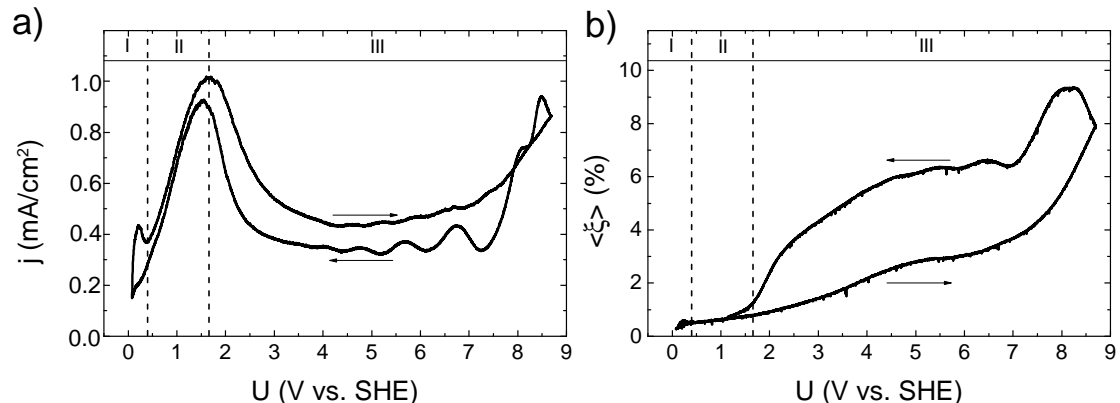


Figure 1: Cyclic voltammogram (left) (20 mV/s) of a highly illuminated n-Si sample (pH=1, $c_F = 75$ mM) and the corresponding, spatially averaged signal of the oxide layer mass ξ (right). The arrows indicate the scan direction.

ca. 0.2 V vs. SHE (part I) the divalent oxidation mechanism dominates [9, 10, 16]. Increasing the voltage the tetravalent mechanism becomes dominant but no stable oxide layer forms as the etching process is faster than the oxidation (part II). At voltages higher than ca. 1.7 V vs. SHE a stable oxide layer forms. This stable oxide layer leads to a decrease in the total current (part III). Starting at ca. 4 V vs. SHE in the upward scan current oscillations can be seen. These oscillations become even more pronounced upon reversal of the scan direction and can also be seen in the mass of the oxide layer, as measured with an ellipsometric setup (see below) and depicted in Fig. 1b. The difference between the current in the upward and the downward scan can be well understood by the corresponding difference in the mass of the oxide layer on the electrode surface inhibiting the current.

2.1 Experimental setup

To study the properties of the oxide layer during the potentiostatic photoelectrodisolution of n-doped silicon, we use a three electrode electrochemical cell equipped with an ellipsometric imaging system providing spatially resolved information on the oxide layer mass as shown in Fig. 2. The polarization of elliptically polarized light incident on the surface is changed upon reflection at the $\text{Si}|\text{SiO}_2|\text{Electrolyte}$ interface and this change is then converted into an intensity signal by a polarizer (blue path in Fig. 2). Insertion of

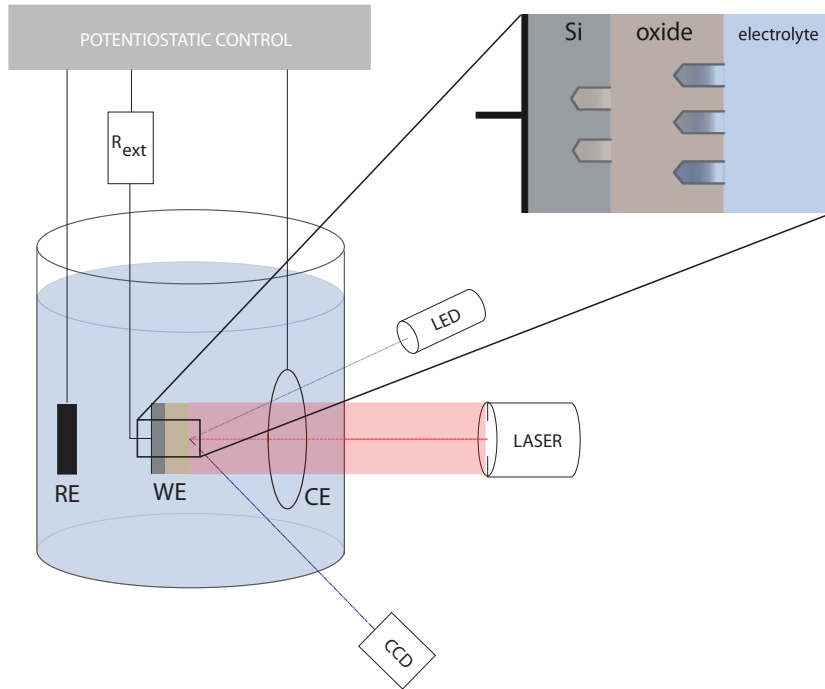


Figure 2: Sketch of the experimental setup showing the arrangement of the three electrodes and the external resistance together with the optical paths for the sample illumination (red) and the spatially resolved ellipsometric imaging (blue). A cross section of the interface and the growth direction of the oxide is shown in the inset.

an imaging optic in the reflected light path gives an image of the electrode on a CCD chip. The system allows the in situ measurement of the optical path through the silicon oxide at a given area on the surface with a spatial resolution in the $10 \mu\text{m}$ range. We call the intensity at each pixel relative to the detection limit of the CCD the ellipsometric intensity ξ . For an optimal contrast an angle of incidence on the sample surface close to the Brewster angle of the Si|Water system (ca. 70°) has to be chosen.

Silicon samples and electrolyte are prepared as described in [17] and the electrolyte is kept under an argon atmosphere throughout the experiments. To minimize parameter variations across the silicon surface the electrolyte solution is constantly stirred. Furthermore, the counter electrode is placed symmetrically opposite the silicon working electrode at a distance of several centimeters to minimize possible coupling effects [18]. Under these conditions perfectly uniform oscillations in ξ can be realized as shown in Fig.(3).

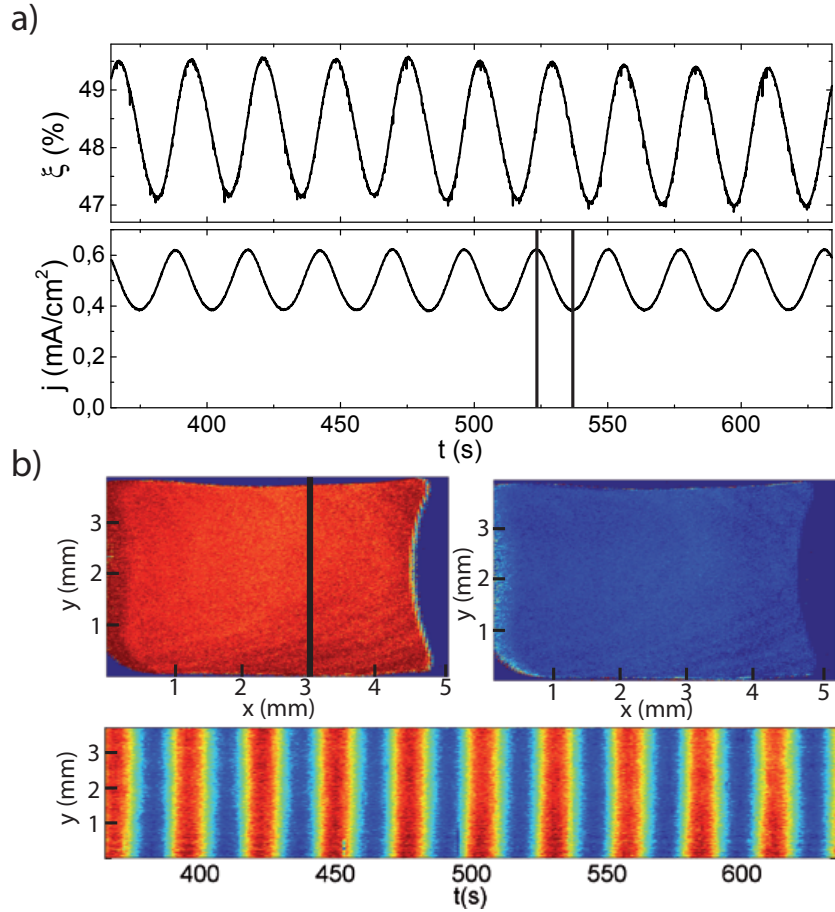


Figure 3: Uniform oscillation of ξ at a high illumination intensity and under constant potential ($c_F = 50$ mM, pH = 2.3, $R_{\text{ext}}A = 2.7$ k Ω cm², $I_{\text{ill}} = 3.0$ mW/cm², $U = 8.65$ V vs. SHE). **a)** Time series of the global quantities ξ and j ; **b)** Ellipsometric intensity distribution on the electrode for the two times indicated in a) and the temporal evolution of a 1d cut along the line indicated in the left electrode picture. Red indicates a relatively high and blue a relatively low value of ξ .

2.2 Dynamics

As early as 1958 it was established that the potentiostatic electrodedissolution of p-doped silicon can proceed in an oscillatory fashion when the applied anodic bias is sufficient [9]. To stabilize the otherwise damped oscillations an external resistor connected in series with the working electrode has been found to be indispensable [19]. This external resistance R_{ext} links the potential drop across the silicon|oxide|electrolyte interface $\Delta\phi_{\text{int}}$ to the total current I passing through the surface.

$$\Delta\phi_{\text{int}} = U - R_{\text{ext}} \cdot I \quad (2)$$

Thus, the external resistance introduces a coupling between all points at the electrode surface. This coupling is both global, as only the spatial average of the current is relevant, and linear. The behavior of the electrodedissolution of n-doped silicon for sufficiently high illumination is identical to that of p-doped silicon [20, 21]. This can be explained by the fact that the amount of holes in the valence band of the silicon is in this case always sufficient to maintain the current determined by the electrochemical parameters. In both cases the oscillations arise from a Hopf bifurcation occurring at a minimal, electrolyte specific threshold value of the external resistance [22] as shown in Fig 4. It is clearly

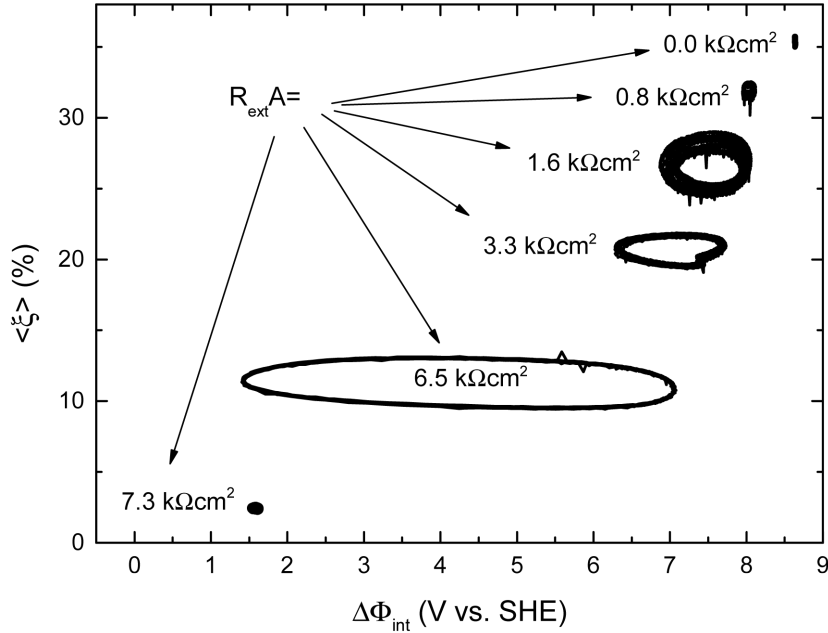


Figure 4: Phase space plots of spatially averaged time series measured during the photoelectrodedissolution of highly illuminated n-doped silicon (pH 1, $c_F = 75 \text{ mM}$, $U = 8.65 \text{ V vs. SHE}$) with varying R_{ext} .

visible that with an increase of the external resistance first stable, sinusoidal oscillations with amplitudes increasing with the external resistance are found. This is the expected behavior close to a Hopf bifurcation. Upon further increase of R_{ext} the shape of the

oscillations then gradually changes towards a more relaxational type. Above another electrolyte specific threshold value of R_{ext} the oscillations vanish abruptly and instead the system relaxes to a stable node. The upper boundary of the oscillatory regime with respect to the external resistance can be well understood by comparing the voltage drop across the interface in this case as shown in Fig. 4 to the CV scan shown in Fig. 1. The latter shows that the value of $\Delta\phi_{\text{int}}$ for R_{ext} above the oscillation boundary is in the voltage region where no stable oxide can form. The extent of the oscillatory regime is thus determined by a Hopf bifurcation at the low coupling limit and a cut-off caused by leaving the experimental parameters for a stable oxide in the high coupling limit.

A second coupling mechanism can be introduced by decreasing the illumination intensity, thus cutting off the total current caused by limiting the generation of holes in the valence band of the n-doped silicon samples. A lower illumination intensity leads to a higher coupling strength. This coupling has a nonlinear characteristic and is at least partly global as the total current, i.e. the current averaged over all points on the surface, is again determining its strength. The cyclic voltammogram changes significantly when this coupling is introduced as shown in Fig. 5 [16], together with corresponding oxide mass changes. Comparing the illumination limited cyclic scans to the unlimited

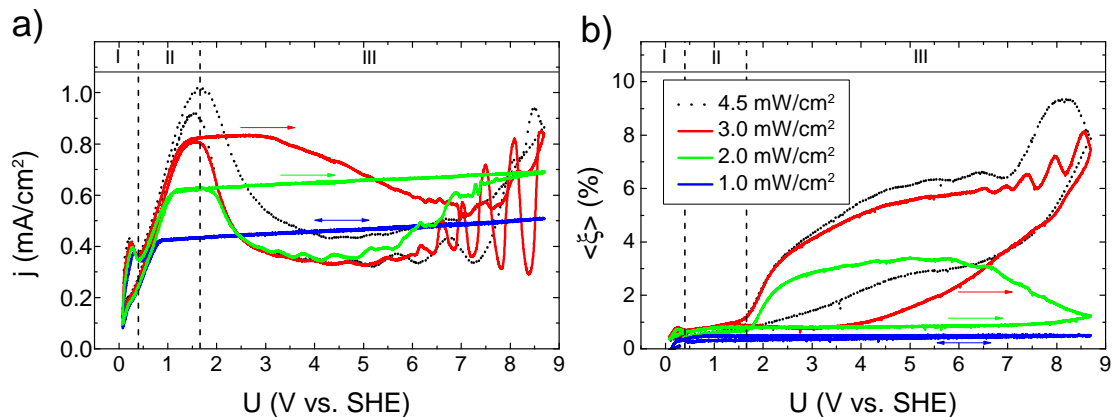


Figure 5: Cyclic voltammogram (left) (20 mV/s) of an n-Si sample (pH=1, $c_F = 75$ mM) at the levels of illumination indicated and the corresponding, spatially averaged signal of the oxide layer mass $\langle \xi \rangle$ (right). The highly illuminated case (dot) is identical to Fig 1.

case, one notes that when the current reaches the illumination limit the oxide growth is initially suppressed. Only at significantly higher potentials does an oxide layer form. The potential shift for the oxide formation is illumination dependent and at too low illumination levels no oxide formation is found at all. In the cases where a stable oxide layer forms, again, both current and oxide layer mass show oscillations. The illumination limitation induced coupling is by itself sufficient to generate sustained oscillations as shown in the phase space plots in Fig 6 Again the coupling strength is also a bifurca-

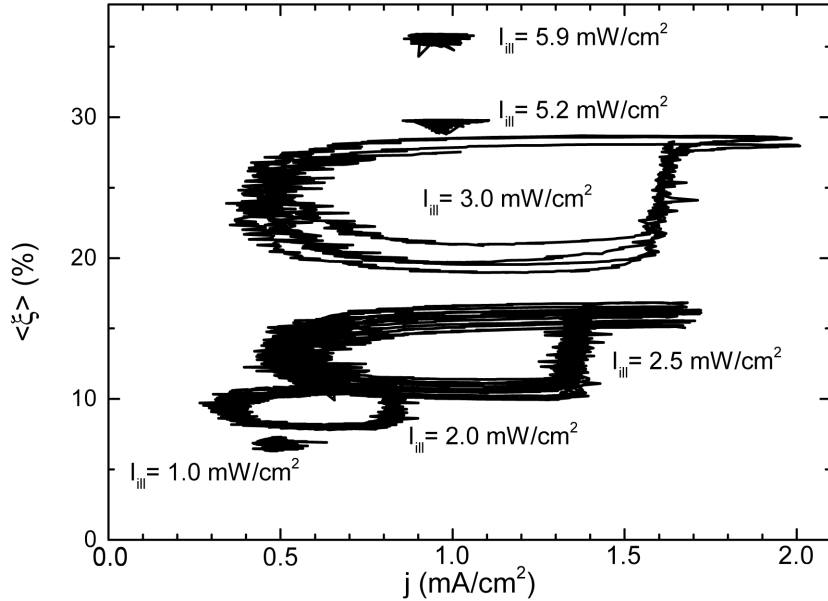


Figure 6: Phase space plots of spatially averaged time series occurring during the photoelectrodissolution of n-doped silicon at various levels of the illumination intensity I_{ill} (pH 1, $c_{\text{F}} = 75$ mM) without an external resistance.

tion parameter leading to stable foci below and stable oscillations above an electrolyte specific threshold value. At very high coupling strength the system relaxes to a stable node. In contrast to the case of the linear global coupling discussed above, however, the transition to the steady state is not abrupt and thus not of the same origin. It is linked to pattern formation and can thus only be understood considering the spatially extended system.

2.3 Spatially extended system

When regarding the spatially extended system an important difference between oscillations stabilized by the linear global coupling and oscillations stabilized by the nonlinear coupling becomes evident. In the former case the oscillations are always spatially uniform, while in the latter case they are often accompanied by pattern formation. This behavior was found in our group purely by chance as an n-doped silicon sample was erroneously used instead of a p-doped one. Unsurprisingly the behavior was quite unexpected and a current could only be seen when the lightproof box in which the experiment resided was opened. Under these conditions the patterns in ξ were first observed. Patterns are also found when the spatially resolved ellipsometric intensity recorded during the cyclic voltammograms shown in Fig. 1 and Fig. 5 is regarded. While in the highly illuminated case, i.e. at negligible nonlinear coupling, oxide growth and also the oscillations in $\langle \xi \rangle$ are spatially uniform, the oxide growth under restricted illumination proceeds along a growing wave front and the oscillations show spatial patterns in ξ . The

nonlinear coupling is thus experimentally indispensable for pattern formation to occur. In experiments with a constant voltage, growing wave fronts are also present in the initial transients preceding the oscillations accompanied by pattern formation. If both coupling mechanisms are combined, pattern formation is found as long as the linear global coupling is not too strong compared to the nonlinear coupling, leading to a typical parameter space as shown in Fig. 7 [21]

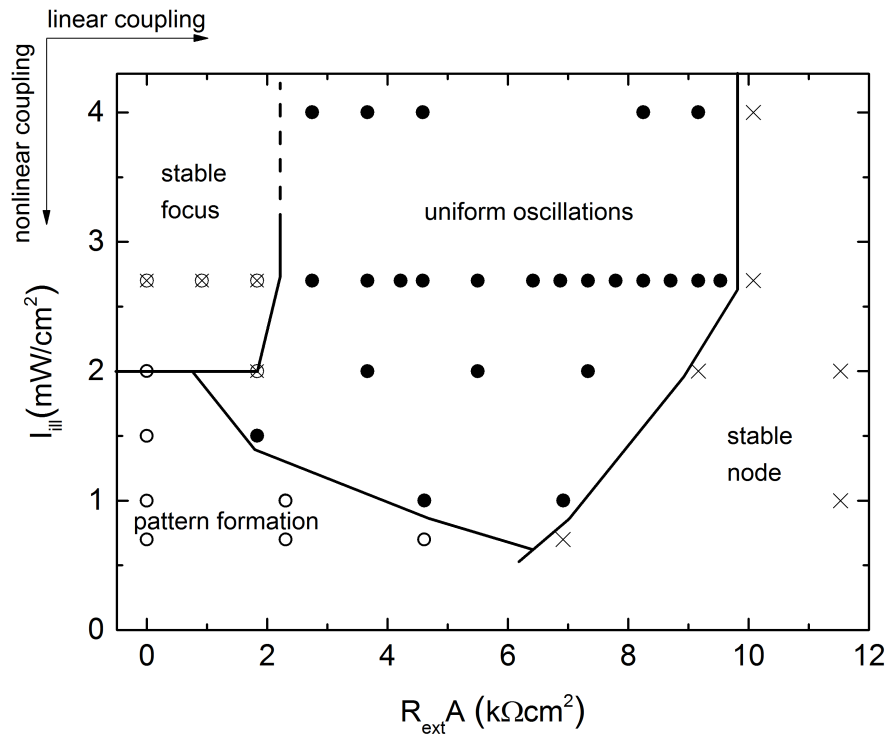


Figure 7: Dependence of the oscillation type on the strengths of the linear, global coupling $R_{\text{ext}} \cdot A$ and the nonlinear coupling, the restriction of I_{III} .

In Section 4 we will present the patterns found in the experiments together with simulation results for a theoretical model system described in what follows.

3 Theoretical modelling of experiments

The experimental system presented in the preceding section can be modelled in a very general way. At high illumination intensities we observe homogeneous oscillations over the entire electrode surface. These oscillations originate in a Hopf bifurcation as described above (see Fig. 6). Thus, in order to model this system, the appropriate normal form to start with is the complex Ginzburg-Landau equation (CGLE) [7, 8, 23] for a complex order parameter $W(\mathbf{x}, t)$

$$\partial_t W = W + (1 + ic_1)\nabla^2 W - (1 + ic_2)|W|^2 W . \quad (3)$$

This equation describes all reaction-diffusion equations in the vicinity of a Hopf bifurcation. For a general derivation see [8]. Equation (3) admits plane wave solutions of wavenumber Q

$$W_Q = a_Q \exp [i(\omega_Q t + Qx)] , \quad (4)$$

with $|a_Q|^2 = 1 - Q^2$ and $\omega_Q = -c_2 + (c_2 - c_1)Q^2$ [8, 23]. A general solution is then given as a combination of these plane waves. This, in general, results in dynamics with an unpreserved homogeneous mode $W_0 = \langle W \rangle$. In contrast, for a huge parameter space the silicon system exhibits conserved harmonic oscillations in the averaged oxide-layer thickness. To achieve this in our model we adjust the CGLE in the most straightforward way by introducing a nonlinear global coupling into Eq. (3), leading to a modified complex Ginzburg-Landau equation (MCGLE) [24, 25]

$$\partial_t W = W + (1 + ic_1)\nabla^2 W - (1 + ic_2)|W|^2 W - (1 + i\nu)\langle W \rangle + (1 + ic_2)\langle |W|^2 W \rangle . \quad (5)$$

Since we model a two-dimensional system, the complex order parameter $W(\mathbf{r}, t)$ is a function of the position vector $\mathbf{r} = (x, y)$ and time t . Angular brackets $\langle \dots \rangle$ denote the spatial average. Now, when taking the spatial average of the whole equation, Eq. (5), one obtains

$$\partial_t \langle W \rangle = -i\nu \langle W \rangle , \quad (6)$$

which results in conserved harmonic oscillations of the spatial average,

$$\langle W \rangle = W_0 = \eta \exp [-i(\nu t + \phi_0)] , \quad (7)$$

with amplitude η and frequency ν . ϕ_0 is an arbitrary initial phase. The essential dynamical properties of the silicon system are thus met with Eq. (5): oscillations arising through a Hopf bifurcation and the conserved harmonic mean-field oscillation. In Section 4 we show that this general ansatz indeed captures the pattern dynamics found in the experiments.

3.1 Clusters

The common notion of phase clusters describes a state, where the oscillatory medium separates into several parts. The oscillations in the different parts are phase shifted with respect to each other [5, 26, 27, 28, 29]. In the most simple case the clusters are arranged symmetrically and therefore the phase shifts in case of n clusters amount to $2\pi m/n$ [30, 28, 29], where $m = 1, 2, \dots, n - 1$. Typically, in the case of cluster patterns the dynamics can be reduced to a phase model. However, there exist a second type of clusters, where essential variations in the amplitudes are present, called type II clusters

[31, 24, 25]. We will see that this second type of cluster patterns naturally arises in our experiments and can be reproduced with the MCGLE.

But first of all we have to clarify, how clustering can occur and why it is possible in the MCGLE. Note that in the CGLE, Eq. (3), cluster patterns cannot emerge, since the dynamics are invariant under a phase shift $W \rightarrow e^{i\chi}W$, for arbitrary χ . For clustering to occur this symmetry has to be broken. This becomes clear when considering two-phase clusters with a period of T_0 and phase balance (i.e. both clusters have the same size). Then, the dynamical equations have to stay invariant only when shifting the time t_0 to $t_0 + T_0/2$, but they are no longer invariant with respect to arbitrary shifts in time. In terms of the complex order parameter W this means that the dynamical equations are only invariant under the discrete transformation

$$W = \hat{W} \exp [i\omega_0 t] \quad \rightarrow \quad \hat{W} \exp [i(\omega_0(t + T_0/2))] . \quad (8)$$

With $\omega_0 = 2\pi/T_0$ the transformation reads

$$W \quad \rightarrow \quad e^{i\pi} W . \quad (9)$$

In general, for n clusters, one needs that the equations are invariant under the discrete symmetry

$$W \quad \rightarrow \quad e^{i2\pi/n} W . \quad (10)$$

To account for this symmetry the proper extension of the CGLE is given by the term $\gamma_n W^{*n-1}$, describing also an external resonant forcing [32, 33, 34, 23, 28, 35, 29, 36, 37, 38]. The asterisk denotes complex conjugation.

We will see that such a symmetry breaking term is intrinsically present in the MCGLE. Therefore, we write $W = W_0(1+w)$ for the complex amplitude in Eq. (5). By exploiting the conservation law, Eq. (7), and the resulting fact that $\langle w \rangle = \langle w^* \rangle = 0$, one obtains again a CGLE, now for the inhomogeneity w , which reads [25]

$$\begin{aligned} \partial_t w = & (\mu + i\beta)w + (1 + ic_1)\nabla^2 w \\ & - (1 + ic_2)\eta^2(|w|^2 w + w^*) + C , \end{aligned} \quad (11)$$

where

$$C = (1 + ic_2)\eta^2 \left[\langle 2|w|^2 + w^2 \rangle - (2|w|^2 + w^2) \right] \quad (12)$$

and $\mu = 1 - 2\eta^2$, $\beta = \nu - 2c_2\eta^2$. Here the needed symmetry-breaking term $-(1 + ic_2)\eta^2 w^*$ occurs. But note that this term does not arise from the nonlinear global coupling. It would be present also when considering the CGLE, Eq. (3), without additional couplings. Crucial are the terms in C proportional to $|w|^2$ and w^2 . As long as they are present, the equation is not symmetric with respect to the transformation $w \rightarrow e^{i\psi}w$ for any ψ . Here the nonlinear global coupling comes into play, as it renders a vanishing C possible, via the term proportional to $\langle 2|w|^2 + w^2 \rangle$. For this case, i.e. for $C = 0$,

the occurrence of clusters is possible and the equation is symmetric with respect to the discrete symmetry $w \rightarrow e^{i\pi}w$. Note that this is impossible for a solely linear global coupling.

4 Results & Discussion

In the following sections we will demonstrate how well the dynamics of the oxide-layer thickness are captured with our very general ansatz in Eq. (5).

4.1 Cluster patterns

As we have clarified the theoretical basis for the emergence of cluster patterns in Section 3.1, we now turn towards the results of our experiments and simulations. In Fig. 8 we compare the cluster dynamics in the simulations of Eq. (5) with the experimental ones [17]. In Fig. 8a and c two-dimensional snapshots of the simulations and the experiments, respectively, are shown. The spatio-temporal dynamics can be seen in one-dimensional cuts in Fig. 8b and d for the simulations and the experiments, respectively. They show that the homogeneous oscillation is modulated by two-phase clusters. Therefore, it is clear, that the phase shift between two regions is not given by π .

To analyze time series of this we perform a Fourier transformation in time at every point \mathbf{r} of the ellipsometric signal and of the real part of $W(\mathbf{r}, t)$ for the experiments and simulations, respectively [24]. We spatially average the resulting amplitudes $|a(\mathbf{r}, \omega)|^2$ to obtain the cumulative power spectrum $S(\omega) = \langle |a(\mathbf{r}, \omega)|^2 \rangle$. Results are shown in Fig. 9.

Two major peaks occur in both cumulative power spectra in Fig. 9a (theory) and d (experiment), one at the frequency ν of the mean-field oscillation. The other one describes the frequency of the clusters. This becomes clear when considering the Fourier amplitudes, corresponding to these peaks, in the complex plane: At $\omega = \nu$ (Fig. 9b and e) all local oscillators form a bunch, while at $\omega \approx \nu/2$ (Fig. 9c and f) the oscillators arrange into two clusters, located at the endpoints of the bar visible. Due to the diffusive coupling, the clusters are connected by an interfacial region, leading to the intermediate oscillators of the bar. The fact that the connection of the two clusters crosses the zero point implies that the borders between them are Ising-type walls. As in this picture the phase shift between the two clusters is given by π , we conclude that at this frequency the clustering takes place. In the experiments in most cases the cluster frequency is given by approximately $\nu/2$. This leads to the conclusion that the clusters arise via a period-doubling bifurcation. Contrarily, in the theory the cluster frequency can be tuned continuously. For better comparison, we chose the parameter values such that the frequency also amounts to $\nu/2$.

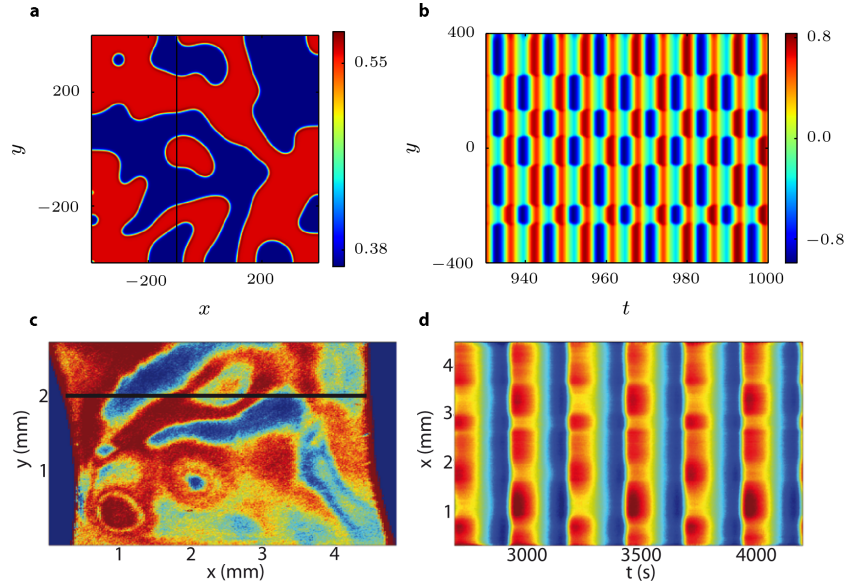


Figure 8: Two-phase clusters in theory (a,b) and experiment (c,d). (a) Snapshot of the two-dimensional oscillatory medium in the theory. Shown is the real part of W . (b) Spatio-temporal dynamics in an one-dimensional cut versus time in the theory. (c,d) The same as (a,b) now for the experimental results. The simulation captures the experimental dynamics very well. Note that the colorbars are different for each subfigure. Parameters read: $c_1 = 0.2$, $c_2 = -0.58$, $\nu = 1.0$, $\eta = 0.66$ (simulation) and $c_F = 35$ mM, pH=1, $R_{\text{ext}} \cdot A = 9.1$ k Ω cm 2 , $I_{\text{ill}} = 0.7$ mW/cm 2 (experiment).

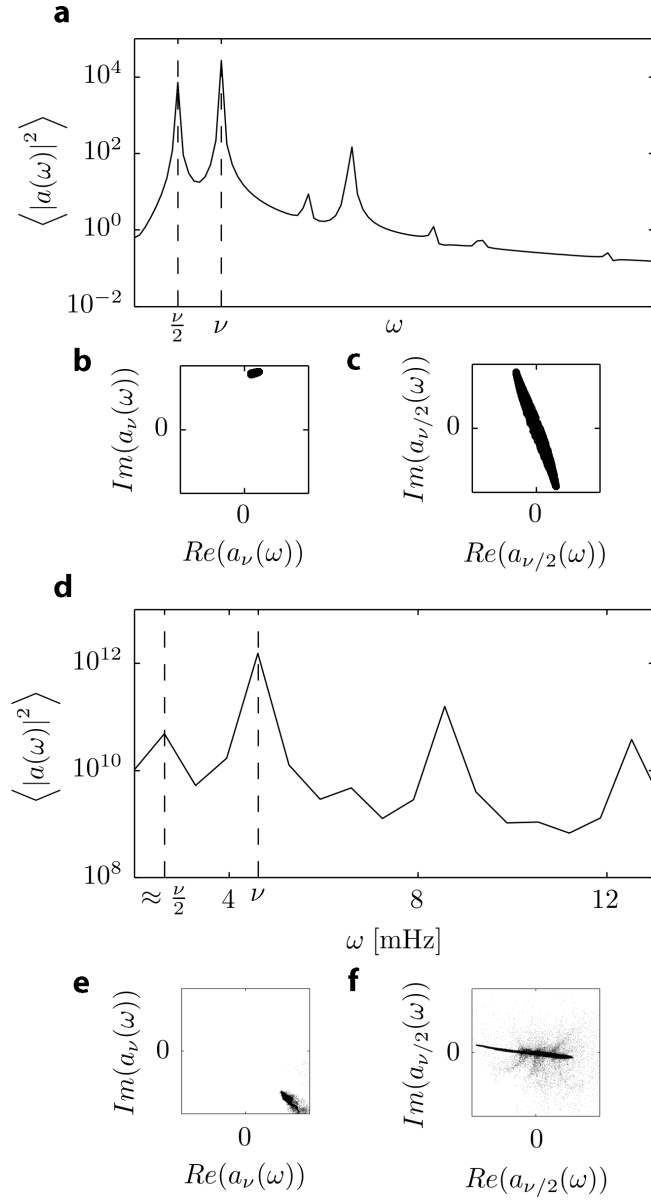


Figure 9: (a,d) Cumulative power spectra for experiments and simulations, respectively. The two major peaks at ν and approximately $\nu/2$ are indicated. The arrangement of the local Fourier amplitudes in the complex plane corresponding to these peaks are depicted in (b) and (c) for the theory and (e) and (f) for the experiments, respectively. The whole two-dimensional system is considered, which leads to the scattered oscillators in the experimental result in (f).

4.2 Subclustering

A symmetry-breaking type of clustering also occurs in our simulations and experiments. The system again separates into two regions as in the case of the two-phase clusters, but now one region is homogeneous, while the other one exhibits two-phase clusters as a substructure [17]. Such states were also observed in Refs. [39, 40]. The results are depicted in Fig. 10.

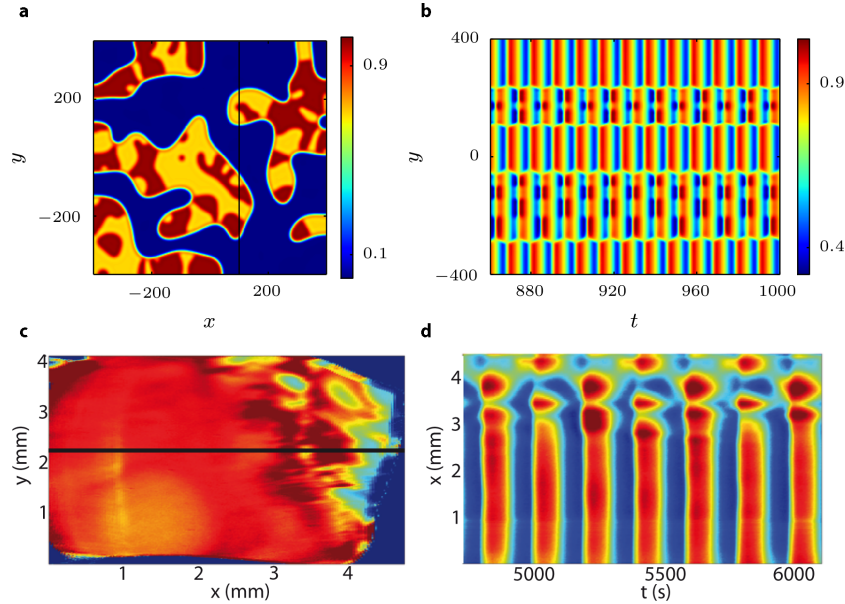


Figure 10: Subclustering in theory (a,b) and experiment (c,d) . Again snapshots (a,c) and one-dimensional cuts (b,d) are shown. The system splits into two regions, one region being homogeneous and one exhibiting two-phase clusters as a substructure. Note that in (b) for better visibility $|W(y,t)|$ is shown. Parameters read: $c_1 = 0.2$, $c_2 = -0.67$, $\nu = 0.1$, $\eta = 0.66$ (simulation) and $c_F = 35$ mM, pH=1, $R_{\text{ext}} \cdot A = 7.6$ k Ω cm 2 , $I_{\text{ill}} = 0.5$ mW/cm 2 (experiment).

In the simulations the two-phase subclusters oscillate at half the frequency of the main clusters. This indicates that the subclustering is connected to a period doubling bifurcation.

4.3 Chimera states

In the preceding section we demonstrated that the symmetry of the two-phase cluster pattern can be broken, resulting in a substructure in one of the two domains. This symmetry-breaking can be even more dramatic: one of the two domains does not exhibit a coherent substructure, it rather displays turbulent dynamics. Thus the whole system separates into two regions, one being synchronized, while the other one displays incoherent and chaotic oscillations. This coexistence of synchrony and asynchrony was

termed a chimera state [41] and many theoretical investigations deal with this topic [42, 41, 43, 44, 45, 46, 47, 48, 49, 50, 17]. Chimera states might be of importance for some peculiar observations in different disciplines, such as the unihemispheric sleep of animals [51, 52], the need for synchronized bumps in otherwise chaotic neuronal networks for signal propagation [53] and the existence of turbulent-laminar patterns in a Couette flow [54]. They could also be realized experimentally in chemical, optical, mechanical and electrochemical systems [40, 55, 56, 57, 17].

In Fig. 11 we present the chimera states found in the simulations (a,b) and in the experiments (c,d) [17].

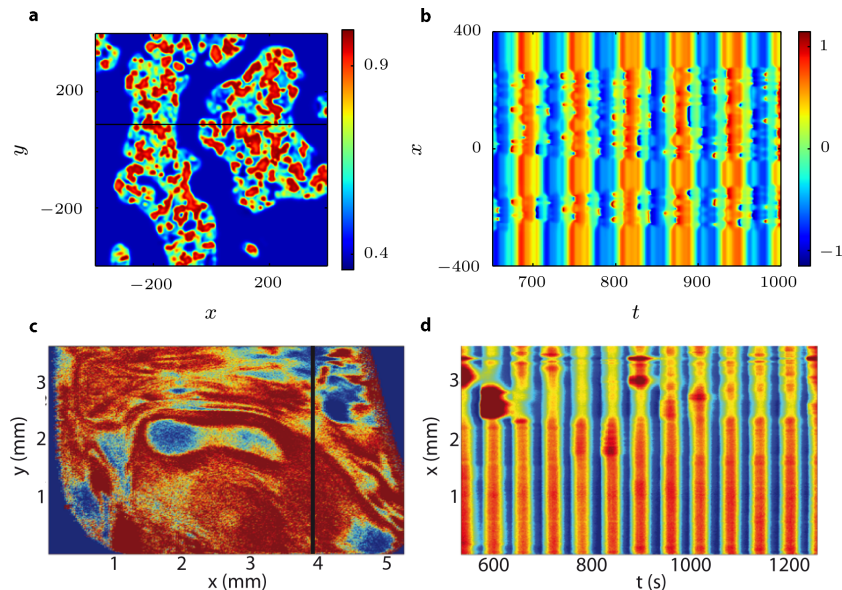


Figure 11: Chimera states in theory (a,b) and experiment (c,d). Snapshots (a,c) and one-dimensional cuts (b,d) are shown. In both, the simulation and the experimental pattern, the synchronized and turbulent regions can be clearly distinguished. Parameters read: $c_1 = 0.2$, $c_2 = -0.58$, $\nu = 0.1$, $\eta = 0.66$ (simulation) and $c_F = 50$ mM, pH=3, $R_{\text{ext}} \cdot A = 4.5$ k Ω cm 2 , $I_{\text{ill}} = 0.5$ mW/cm 2 (experiment).

In both the experiments and the simulations nothing is imposed to induce this symmetry-breaking. The experimental conditions are kept uniform over the entire electrode. Furthermore, these patterns form spontaneously, i.e. no specially prepared initial conditions are required to obtain them. We could show in Ref. [17] that these peculiar dynamics can be traced back to the nonlinear global coupling. In order to proof this, we performed simulations of Eq. (5) without the diffusive coupling, which means that we dealt with an ensemble of Stuart-Landau oscillators coupled solely via the nonlinear global coupling present in Eq. (5). Also in this system the chimera state arises and has the same features as the one presented here. Thus, contrarily to the convincement in literature that a nonlocal coupling is indispensable for the emergence of chimera states, the

chimera state found in our simulations forms under a solely global coupling. The diffusive coupling leads to the spatial arrangement into synchronized and incoherent regions. In the experiments a nonlocal contribution of the nonlinear coupling could not be ruled out yet. However, the striking similarity between simulations and experiments strongly corroborates the notion that the nonlinear coupling acts essentially globally.

4.4 Turbulence

As the coexistence of synchrony and turbulence in the chimera state suggests, we find these states in parameter space between the fully synchronized and the turbulent states. Therefore, the chimera state is kind of an mediator between synchrony and turbulence. An experimental example of the synchronized state is shown in Fig. 3, whereas the turbulent dynamics are presented in Fig. 12.

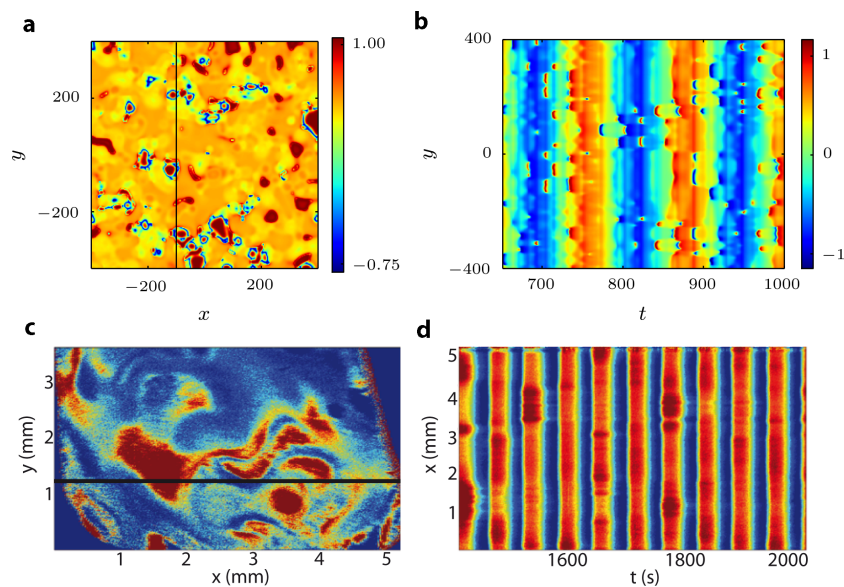


Figure 12: Turbulent dynamics in theory (a,b) and experiment (c,d). Snapshots (a,c) and one-dimensional cuts (b,d) are shown. The whole system exhibits turbulent dynamics. Parameters read: $c_1 = 0.2$, $c_2 = -0.58$, $\nu = 0.05$, $\eta = 0.66$ (simulation) and $c_F = 50$ mM, pH=3, $R_{\text{ext}} \cdot A = 6.7$ k Ω cm 2 , $I_{\text{ill}} = 1.0$ mW/cm 2 (experiment).

A uniform oscillation is still present in dynamics, but it is modulated by incoherent and aperiodic oscillations. Similar turbulent patterns have been found in Ref. [5], where also localized clusters are discussed, which are reminiscent of the subclusters presented in Fig. 10.

5 Conclusions & Outlook

The oscillatory photoelectrodissolution of n-type silicon is a convenient experimental model system exhibiting a wide variety of dynamical states. Most importantly, the formation of many qualitatively different patterns is observed while the spatial average of the oscillations is simple periodic. This behavior can be well reproduced in theoretical simulations using a general normal form approach close to the Hopf bifurcation adjusted to capture the mean-field oscillation.

In the experiments, the points at the electrode surface are coupled by a linear global coupling and a nonlinear coupling both linked to the total current through the electrode surface. In the theoretical modelling this is reflected by the introduction of a nonlinear, purely global coupling. Although the details of the couplings introduced in experiment and theory are different, the results show striking similarities which led us to the conclusion that the observed phenomena are dynamical in origin and robust. Furthermore, it strongly suggests that the nonlinear coupling introduced in the experiments by the insufficient illumination is essentially global and that, e.g., the diffusion length of the minority charge carriers in the silicon plays an only minor role. An important point that might be counterintuitive at first glance, is the nature of the patterns emerging spontaneously in this purely globally coupled system. They often consist of distinct regions showing remarkably different dynamical behavior, the most astonishing example being the chimera state. Global couplings occur naturally in oscillatory systems in many fields of research [58, 59, 60, 61]. The variety of dynamical patterns observed and their spontaneous emergence in the presented experimental system thus offers intriguing insight into the dynamical possibilities of a wide variety of systems.

Acknowledgments

The authors gratefully acknowledge financial support from the *Deutsche Forschungsgemeinschaft* (Grant no. KR1189/12-1), the *Institute for Advanced Study, Technische Universität München* funded by the German Excellence Initiative and the cluster of excellence *Nanosystems Initiative Munich (NIM)*.

References

- [1] J. Lechleiter, S. Girard, E. Peralta, and D. Clapham. Spiral calcium wave propagation and annihilation in *Xenopus laevis* oocytes. *Science*, 252(5002):123–126, 1991.
- [2] A. T. Winfree. Electrical turbulence in three-dimensional heart muscle. *Science*, 266(5187):1003–1006, 1994.
- [3] E. M. Cherry and F. H. Fenton. Visualization of spiral and scroll waves in simulated and experimental cardiac tissue. *New Journal of Physics*, 10(12):125016, 2008.

- [4] G. Ertl. Oscillatory kinetics and spatio-temporal self-organization in reactions at solid surfaces. *Science*, 254(5039):1750–1755, 1991.
- [5] V. K. Vanag, L. Yang, M. Dolnik, A. M. Zhabotinsky, and I. R. Epstein. Oscillatory cluster patterns in a homogeneous chemical system with global feedback. *Nature*, 406:389–391, 2000.
- [6] Irving R. Epstein and Kenneth Showalter. Nonlinear chemical dynamics: Oscillations, patterns, and chaos. *The Journal of Physical Chemistry*, 100(31):13132–13147, 1996.
- [7] Igor S. Aranson and Lorenz Kramer. The world of the complex Ginzburg-Landau equation. *Rev. Mod. Phys.*, 74:99–143, Feb 2002.
- [8] Y. Kuramoto. *Chemical Oscillations, Waves, and Turbulence*. Dover Publications, Inc., Mineola, New York, 2003.
- [9] Dennis R. Turner. Electropolishing silicon in hydrofluoric acid solutions. *J. Electrochem. Soc.*, 105:402–408, 1958.
- [10] R. Memming and G. Schwandt. Anodic dissolution of silicon in hydrofluoric acid solutions. *Surf. Science*, 4:109–124, 1966.
- [11] D. J. Blackwood, A. Borazio, R. Greef, L. M. Peter, and J. Stuper. Electrochemical and optical studies of silicon dissolution in ammonium fluoride solutions. *Electrochimica Acta*, 37:889–896, 1992.
- [12] Konrad Schönleber and Katharina Krischer. High-amplitude versus low-amplitude current oscillations during the anodic oxidation of p-type silicon in fluoride containing electrolytes. *ChemPhysChem*, 13:2989–2996, 2012.
- [13] H. Hasegawa, S. Arimoto, J. Nanjo, H. Yamamoto, and H. Ohno. Anodic oxidation of hydrogenated amorphous silicon and properties of oxide. *J. Electrochem. Soc.*, 135(2):424, 1988.
- [14] M. Matsumura and S. R. Morrison. Anodic properties of n-Si and n-Ge electrodes in HF solution under illumination and in the dark. *J. Electroanal. Chem.*, 147:157–166, 1983.
- [15] S. Cattarin, I. Frateur, M. Musiani, and B. Tribollet. Electrodissolution of p-Si in acidic fluoride media: Modeling of the steady state. *J. Electrochem. Soc.*, 147:3277–3282, 2000.
- [16] M. J. Eddowes. Anodic dissolution of p-type and n-type silicon - kinetic study of the chemical mechanism. *Journal of Electroanalytical Chemistry*, 280 (2):297, 1990.
- [17] Lennart Schmidt, Konrad Schönleber, Katharina Krischer, and Vladimir García-Morales. Coexistence of synchrony and incoherence in oscillatory media under nonlinear global coupling. *Chaos: An Interdisciplinary Journal of Nonlinear Science*, 24(1):013102, 2014.

- [18] Nadia Mazouz, Georg Flätgen, and Katharina Krischer. Tuning the range of spatial coupling in electrochemical systems: From local via nonlocal to global coupling. *Phys. Rev. E*, 55:2260–2266, Mar 1997.
- [19] J. N. Chazalviel, F. Ozanam, M. Etman, F. Paolucci, L. M. Peter, and J. Stumper. The p-Si/fluoride interface in the anodic region: Damped and/or sustained oscillations. *J. Electroanal. Chem.*, 327(1-2):343–349, 1992.
- [20] F. Paolucci, L.M. Peter, and J. Stumper. Wavelength-dependent photocurrent multiplication during the anodic dissolution of n-si in ammonium fluoride solutions. *J. Electroanal. Chem.*, 341:165, 1992.
- [21] K. Schönleber, C. Zensen, A. Heinrich, and K. Krischer. Pattern formation during the oscillatory photoelectrodissolution of n-type silicon: Turbulence, clusters and chimeras. *arXiv:1403.4825*.
- [22] I. Miethe and K. Krischer. Ellipsomicroscopic studies of the anodic oxidation of p-type silicon in fluoride containing electrolytes during current oscillations. *J. Electroanal. Chem.*, 666:1, 2012.
- [23] Vladimir García-Morales and Katharina Krischer. The complex Ginzburg–Landau equation: an introduction. *Contemporary Physics*, 53(2):79–95, 2012.
- [24] Iljana Miethe, Vladimir García-Morales, and Katharina Krischer. Irregular subharmonic cluster patterns in an autonomous photoelectrochemical oscillator. *Phys. Rev. Lett.*, 102:194101, May 2009.
- [25] Vladimir García-Morales, Alexander Orlov, and Katharina Krischer. Subharmonic phase clusters in the complex Ginzburg-Landau equation with nonlinear global coupling. *Phys. Rev. E*, 82:065202, Dec 2010.
- [26] Vladimir K. Vanag, Anatol M. Zhabotinsky, and Irving R. Epstein. Pattern formation in the Belousov-Zhabotinsky reaction with photochemical global feedback. *J. Phys. Chem. A*, 104(49):11566–11577, 2000.
- [27] Alexander S. Mikhailov and Kenneth Showalter. Control of waves, patterns and turbulence in chemical systems. *Physics Reports*, 425(2–3):79 – 194, 2006.
- [28] Anna L. Lin, Aric Hagberg, Ehud Meron, and Harry L. Swinney. Resonance tongues and patterns in periodically forced reaction-diffusion systems. *Phys. Rev. E*, 69:066217, Jun 2004.
- [29] Prabha Kaira, Pablo S. Bodega, Christian Punckt, Harm Hinrich Rotermund, and Dagmar Krefting. Pattern formation in 4:1 resonance of the periodically forced CO oxidation on Pt(110). *Phys. Rev. E*, 77:046106, Apr 2008.
- [30] Koji Okuda. Variety and generality of clustering in globally coupled oscillators. *Physica D: Nonlinear Phenomena*, 63(3–4):424 – 436, 1993.

- [31] Hamilton Varela, Carsten Beta, Antoine Bonnefont, and Katharina Krischer. A hierarchy of global coupling induced cluster patterns during the oscillatory H₂-electrooxidation reaction on a Pt ring-electrode. *Phys. Chem. Chem. Phys.*, 7:2429–2439, 2005.
- [32] J. M. Gambaudo. Perturbation of a Hopf bifurcation by an external time-periodic forcing. *J. Diff. Eqs.*, 57:172, 1985.
- [33] Pierre Couillet and Kjartan Emilsson. Strong resonances of spatially distributed oscillators: a laboratory to study patterns and defects. *Physica D: Nonlinear Phenomena*, 61(1–4):119 – 131, 1992.
- [34] V. Petrov, Q. Ouyang, and H. L. Swinney. Resonant pattern formation in a chemical system. *Nature*, 388:655–657, 1997.
- [35] A. Yochelis, C. Elphick, A. Hagberg, and E. Meron. Frequency locking in extended systems: The impact of a Turing mode. *EPL (Europhysics Letters)*, 69(2):170, 2005.
- [36] Jessica M. Conway and Hermann Riecke. Multiresonant forcing of the complex Ginzburg-Landau equation: Pattern selection. *Phys. Rev. E*, 76:057202, Nov 2007.
- [37] B. Marts, A. Hagberg, E. Meron, and A. L. Lin. Resonant and nonresonant patterns in forced oscillators. *Chaos*, 16:037113, 2006.
- [38] Arik Yochelis, Christian Elphick, Aric Hagberg, and Ehud Meron. Two-phase resonant patterns in forced oscillatory systems: boundaries, mechanisms and forms. *Physica D: Nonlinear Phenomena*, 199(1–2):201 – 222, 2004. Trends in Pattern Formation: Stability, Control and Fluctuations.
- [39] Kuniyuki Kaneko. Clustering, coding, switching, hierarchical ordering, and control in a network of chaotic elements. *Physica D: Nonlinear Phenomena*, 41(2):137 – 172, 1990.
- [40] Mark R Tinsley, Nkomo Simbarashe, and Kenneth Showalter. Chimera and phase-cluster states in populations of coupled chemical oscillators. *Nature Phys.*, 8:662–665, Jul 2012.
- [41] Daniel M. Abrams and Steven H. Strogatz. Chimera states for coupled oscillators. *Phys. Rev. Lett.*, 93:174102, Oct 2004.
- [42] Y. Kuramoto and D. Battogtokh. Coexistence of coherence and incoherence in nonlocally coupled phase oscillators. *Nonlin. Phenom. in Complex Syst.*, 5:380–385, 2002.
- [43] Shin-ichiro Shima and Yoshiki Kuramoto. Rotating spiral waves with phase-randomized core in nonlocally coupled oscillators. *Phys. Rev. E*, 69:036213, Mar 2004.

- [44] Erik A. Martens, Carlo R. Laing, and Steven H. Strogatz. Solvable model of spiral wave chimeras. *Phys. Rev. Lett.*, 104:044101, Jan 2010.
- [45] Gautam C. Sethia, Abhijit Sen, and Fatihcan M. Atay. Clustered chimera states in delay-coupled oscillator systems. *Phys. Rev. Lett.*, 100:144102, Apr 2008.
- [46] Daniel M. Abrams, Rennie Mirollo, Steven H. Strogatz, and Daniel A. Wiley. Solvable model for chimera states of coupled oscillators. *Phys. Rev. Lett.*, 101:084103, Aug 2008.
- [47] Iryna Omelchenko, Yuri Maistrenko, Philipp Hövel, and Eckehard Schöll. Loss of coherence in dynamical networks: Spatial chaos and chimera states. *Phys. Rev. Lett.*, 106:234102, Jun 2011.
- [48] Iryna Omelchenko, Bruno Riemenschneider, Philipp Hövel, Yuri Maistrenko, and Eckehard Schöll. Transition from spatial coherence to incoherence in coupled chaotic systems. *Phys. Rev. E*, 85:026212, Feb 2012.
- [49] Simbarashe Nkomo, Mark R. Tinsley, and Kenneth Showalter. Chimera states in populations of nonlocally coupled chemical oscillators. *Phys. Rev. Lett.*, 110:244102, Jun 2013.
- [50] Iryna Omelchenko, Oleh E. Omel'chenko, Philipp Hövel, and Eckehard Schöll. When nonlocal coupling between oscillators becomes stronger: Patched synchrony or multichimera states. *Phys. Rev. Lett.*, 110:224101, May 2013.
- [51] N. C. Rattenborg, C. J. Amlaner, and S. L. Lima. Behavioral, neurophysiological and evolutionary perspectives on unihemispheric sleep. *Neurosc. and Biobehav. Rev.*, 24:817–842, 2000.
- [52] Christian G. Mathews, John A. Lesku, Steven L. Lima, and Charles J. Amlaner. Asynchronous eye closure as an anti-predator behavior in the western fence lizard (*sceloporus occidentalis*). *Ethology*, 112:286–292, 2006.
- [53] Tim P. Vogels, Kanaka Rajan, and L. F. Abbott. Neural network dynamics. *Annu. Rev. Neurosci.*, 28:357–376, 2005.
- [54] Dwight Barkley and Laurette S. Tuckerman. Computational study of turbulent laminar patterns in Couette flow. *Phys. Rev. Lett.*, 94:014502, Jan 2005.
- [55] Aaron M. Hagerstrom, Thomas E. Murphy, Rajarshi Roy, Philipp Hövel, Iryna Omelchenko, and Eckehard Schöll. Experimental observation of chimeras in coupled-map lattices. *Nature Phys.*, 8:658–661, Jul 2012.
- [56] Erik Andreas Martens, Shashi Thutupalli, Antoine Fourrière, and Oskar Halatschek. Chimera states in mechanical oscillator networks. *Proc. Natl. Acad. Sci.*, 110(26):10563–10567, 2013.

- [57] Mahesh Wickramasinghe and István Z. Kiss. Spatially organized dynamical states in chemical oscillator networks: Synchronization, dynamical differentiation, and chimera patterns. *PLoS ONE*, 8(11):e80586, 11 2013.
- [58] H.-G. Purwins, H. U. Bödeker, and S. Amiranashvili. Dissipative solitons. *Adv. in Phys.*, 59:485, 2010.
- [59] K. Krischer. Nonlinear dynamics in electrochemical systems. In R. C. Alkire and D. M. Kolb, editors, *Advances in Electrochemical Science and Engineering*, volume 8, pages 89–208. 2003.
- [60] Steven H. Strogatz. From Kuramoto to Crawford: exploring the onset of synchronization in populations of coupled oscillators. *Physica D: Nonlinear Phenomena*, 143(1–4):1 – 20, 2000.
- [61] A. Wacker and E. Schöll. Criteria for stability in bistable electrical devices with S- or Z-shaped current voltage characteristic. *Journal of Applied Physics*, 78(12):7352–7357, 1995.